

Abstract A spectral solution method is proposed to solve a previously developed non-equilibrium statistical model describing partial thermalization of produced charged hadrons in relativistic heavy-ion collisions, thus improving the accuracy of the numerical solution. The particle's phase-space trajectories are treated as a drift-diffusion stochastic process, leading to a Fokker–Planck equation (FPE) for the single-particle probability distribution function. The drift and diffusion coefficients are derived from the expected asymptotic states via appropriate fluctuation–dissipation relations, and the resulting FPE is then solved numerically using a spectral eigenfunction decomposition. The calculated time-dependent particle distributions are compared to Pb-Pb data from the ATLAS and ALICE collaborations at the Large Hadron Collider.

PACS 25.75.-q, Relativistic heavy-ion collisions · 25.75.Ag Global features in relativistic heavy-ion collisions · 25.75.Dw Particle and resonance production · 02.30.Mv Approximations and expansions · 02.70.Hm Spectral methods

Spectral eigenfunction decomposition of a Fokker–Planck operator for relativistic heavy-ion collisions

A. Rizzi · G. Wolschin

Received: date / Revised version: date

1 Introduction

Relativistic heavy-ion collisions [1] are a versatile tool to study the partial approach of a quantum many-body system towards statistical equilibrium. To account for time-dependent charged-hadron production at energies reached at the Relativistic Heavy Ion Collider RHIC and the Large Hadron Collider LHC, an explicit and rigorous derivation of the Fokker–Planck equation (FPE) for the momentum distribution function in longitudinal and transverse rapidities has recently been given [2]. Using the mathematics of stochastic calculus, the relativistic diffusion model (RDM, [3, 4, 5]) could thus be placed on a firm nonequilibrium-statistical foundation. In particular, the model has been used to analyze charged-hadron production in Pb-Pb collisions at LHC energies, and detailed comparisons of both marginal and joint particle distributions with charged-hadron data in transverse-momentum and pseudorapidity space from the ATLAS and ALICE collaborations have been performed. We now extend this work using an algebraic solution method that is based on a spectral eigenfunction decomposition of the Fokker–Planck operator, and promises higher accuracy at larger transverse momenta.

The relativistic diffusion model’s scope is located between the equilibrium-statistical models for multiple hadron production that were originally proposed by Fermi [6] and Hagedorn [7], and more detailed and complicated numerical nonequilibrium models that not only provide a QCD-based description of the initial stages of the collision – such as the Color Glass Condensate (CGC, see [8]) –, but use viscous relativistic hydrodynamics for the main part of the time evolution

(e.g. [9, 10, 11, 12, 13, 14]), and codes like URQMD for the hadronic final-state interactions [15].

While in most of the available theories of relativistic heavy-ion collisions, charged-hadron production is considered to occur from the hot fireball of partons that expands, cools, and eventually hadronizes in a parton-hadron crossover, the RDM with three sources [16] also accounts for the contribution from the highly excited fragments to particle production. The role of these additional sources, which are clearly visible in net-baryon (*stopping*) distributions at the Super Proton Synchrotron SPS and RHIC, has been considered in a model that relies on the interaction of valence quarks with soft gluons in the respective other nucleus and is based on gluon-saturation physics [17, 18]. It has later been incorporated into a nonequilibrium-statistical approach that also accounts for the time-dependence of the stopping process [19]. Here, the gluon-gluon source does not contribute, because it produces particles and antiparticles in equal amounts.

In particle production at energies reached at RHIC and LHC, however, the central fireball becomes the main source. The initial state is derived from quantum chromodynamics (QCD) within the color-glass model and evolved in time with a cylindrically symmetric FPE in longitudinal and transverse momentum space constructed via the appropriate fluctuation-dissipation relation (FDR), that connects the drift and diffusion coefficients with the expected asymptotic state [2]. The majority of the produced hadrons participate in the thermalization process, but since the system is not spatially confined, it cannot reach a true thermal equilibrium that is stationary in position space and independent of its initial state. Therefore, the asymptotic particle distribution function is expected to be a modified thermal distribution that exhibits a collective expansion of

the system, reminiscent of its initial configuration. Although a correct description of the asymptotic state is crucial in the model to mesoscopically derive the form of the FPE, the system never completes the thermalization process due to a "freeze out" of strong interactions, and charged hadrons remain far from equilibrium in the longitudinal degrees of freedom at the time they are detected.

Analytical solutions of the relativistic diffusion model [3] with simplified transport coefficients have been successfully compared to LHC spectra [16, 5]. When solving the FPE for a two-dimensional diffusion tensor and the associated rapidity-dependent drift, however, the accuracy of the finite-difference numerical method prevented the comparison to experimental data at large transverse momenta, where the particle yield is small compared to the peak of the distribution, but measured with high accuracy [2]. It is the first motivation of the present work to explore the applicability of a spectral eigenfunction solution of the FPE, and investigate whether the method is suitable for particle production from both, fireball and fragmentation sources. We also investigate the effect of a dependence of the diffusion coefficient on longitudinal rapidity y . The second aim is to possibly increase the numerical accuracy at larger transverse momenta through the use of this new solution method.

The FPE as derived from stochastic calculus in the context of longitudinal and transverse degrees of freedom of quasi-particles in relativistic heavy-ion collisions [2] requires as a necessary condition for its validity the presence of a fluctuating background that is provided by the partons in the participating nucleons. Contrary to common belief, a heat bath with temperature T as in classical Brownian motion of a heavy particle of mass M , and the corresponding restriction $M \gg T$ is not needed. As a caveat, it is mentioned that in cases where the widths of the quasi-particles become comparable to or larger than their masses – which may be the case for pions and kaons considered in this paper –, the theoretical justification of the approach may be limited in spite of its empirical success. However, reliable calculations of the in-medium widths for light hadrons produced at LHC energies do not seem to be available.

In the following section, the relativistic diffusion model for charged-hadron production [2, 3] in longitudinal and transverse momentum space is briefly reviewed. We discuss the spectral method used for solving the FPE, and the applicability of the method for the central and the fragmentation sources, in Sect. 3. A comparison of the model results to ALICE [20, 21, 22] and ATLAS [23] measurements of central Pb-Pb collisions with $\sqrt{s_{\text{NN}}} = 2.76$ and 5.02 TeV is given in Sect. 4, where the free parameters are determined in χ^2 minimizations.

Extrapolating the parameters to $\sqrt{s_{\text{NN}}} = 5.36$ TeV allows us to make a prediction for the LHC Run 3 at this energy. We discuss the results, suggest improvements of the model, and possible future outcomes of the research in the concluding Sect. 5.

2 Relativistic diffusion model

Generalizing the concept of relativistic Brownian motion [24, 25, 26], we model the charged-particle trajectories in a relativistic heavy-ion collision as stochastic drift-diffusion processes [2]. As a consequence of the fundamental mathematical principle that stochastic processes in position space cannot be both Lorentz-invariant and (first-order) Markovian [27, 28, 29], the trajectories are expressed with respect to the Brownian particle's phase-space configuration (\mathbf{x}, \mathbf{p}) instead of merely its position \mathbf{x} . When including the particle's momenta \mathbf{p} in the definition of the trajectory, the resulting drift-diffusion process is second-order Markovian in position-space coordinates, thus keeping the beneficial mathematical properties of Markov processes.

Denoting the probabilistic trajectories of the Brownian particle in position and momentum space as $\mathbf{X} = (X^1, X^2, X^3)$ and $\mathbf{P} = (P^1, P^2, P^3)$, respectively, the increments $dX^\mu(t) := X^\mu(t + dt) - X^\mu(t)$ of the position-space trajectory due to an infinitesimal timestep dt in the laboratory frame obey the stochastic differential equation (SDE)

$$dX^\mu(t) = \frac{P^\mu(t)}{P^0(t)} dt \quad \text{for } \mu = 0, \dots, 3. \quad (1)$$

The particle's energy is determined by the mass-shell condition

$$P^0(t) := \sqrt{m^2 + \sum_{i=1}^3 P^i(t)^2}, \quad (2)$$

where the 3-axis is parallel to the beam axis so that x^1 and x^2 span the transverse plane.

The time-evolution of the particle's momentum \mathbf{P} is taken to follow a drift-diffusion SDE,

$$dP^i(t) = \mu_{\mathbf{P}}^i(\mathbf{P}(t)) dt + \sum_{k=1}^3 \sigma_{\mathbf{P}}^{ik}(\mathbf{P}(t)) dW^k(t) \quad \text{for } i = 1, 2, 3, \quad (3)$$

with a 3-dimensional drift coefficient $\mu_{\mathbf{P}}$ and a (3×3) -dimensional diffusion coefficient $\sigma_{\mathbf{P}}$ representing generalized directed (deterministic) and undirected (stochastic) forces, respectively. A three-dimensional standard Wiener process $\mathbf{W}(t)$ – the mathematical formulation of Gaussian white noise – represents the stochastic forces.

In Eq. (3), drift and diffusion are assumed to be independent of the particle's position $\mathbf{X}(t)$. The time-evolution of the system can then be accounted for as a momentum-space process \mathbf{P} , so that the position-space process \mathbf{X} can be disregarded.

In the present work, we only consider central heavy-ion collisions with small impact parameter, equivalent to centrality $< 5\%$. Here, the system has an approximate rotational symmetry with respect to the beam axis: it is effectively two-dimensional when expressed in terms of transverse momentum $p_\perp := \sqrt{(p^1)^2 + (p^2)^2}$ and longitudinal momentum $p_\parallel := p^3$. The transverse-plane angular coordinate can then be eliminated, resulting in a two-dimensional drift-diffusion SDE. A hyperbolic transformation yields the coordinates transverse and longitudinal rapidity, respectively, with their connection to the transverse and longitudinal momentum

$$h := \sinh^{-1}(p_\perp/m) \quad \text{and} \quad y := \tanh^{-1}(p_\parallel/E). \quad (4)$$

The transverse rapidity h maps low p_\perp to a linear and high p_\perp to a logarithmic scale, and the particle's transverse mass is $m \cosh(h) = \sqrt{m^2 + p_\perp^2} =: m_\perp$. The dynamics of the system is then determined by the functional form of the drift and diffusion coefficients. The drift coefficient can be derived from the time-asymptotic equilibrium distribution of the system. This is conveniently done in the distribution-function representation. The probability density function (PDF) in phase space is obtained through a Kramers–Moyal expansion that yields a Fokker–Planck equation (FPE), which can be converted to a FPE in rapidity space $\xi = (h, y)$ [2]

$$[\partial_t - L_\Xi(\xi)] f_{\Xi(t)}(\xi) = 0 \quad (5)$$

where $\Xi = (H, Y)$ and the rapidity-space Fokker–Planck operator (FPO) is

$$L_\Xi(\xi) = \sum_{i=1}^2 \partial_{\xi^i} \left[-\mu_\Xi^i(\xi) + \sum_{k=1}^2 \partial_{\xi^k} D_\Xi^{ik} \right]. \quad (6)$$

Here, the two diffusion coefficients have been combined into the (2×2) -dimensional diffusivity of Ξ , which is given by

$$D_\Xi^{ik} := \frac{1}{2} \sum_{l=1}^2 \sigma_\Xi^{il} \sigma_\Xi^{kl} \quad \text{for } i, k = 1, 2. \quad (7)$$

By assuming that the system is in detailed balance, the particle distribution will approach an equilibrium state – that need not necessarily be thermal, but can be any time-asymptotic stationary state, $\lim_{t \rightarrow \infty} f_{\Xi(t)}(\xi) \equiv$

$f_{\Xi_{\text{equ}}}(\xi)$. Hence, drift and diffusivity fulfill the fluctuation–dissipation relation

$$\mu_\Xi^i(\xi) = \sum_{k=1}^2 \left[\partial_{\xi^k} D_\Xi^{ik} - D_\Xi^{ik} \partial_{\xi^k} \Phi_\Xi(\xi) \right], \quad (8)$$

with the generalized potential

$$\Phi_\Xi(\xi) := -\ln(f_{\Xi_{\text{equ}}}(\xi)). \quad (9)$$

If the diffusion tensor is chosen to be diagonal and constant in the rapidity variables h and y as in our previous work [2], the FPO decomposes into a transverse and longitudinal part

$$L_\Xi(\xi) = D_\perp \partial_h \left[\frac{\partial \Phi_\Xi(\xi)}{\partial h} + \partial_h \right] + D_\parallel \partial_y \left[\frac{\partial \Phi_\Xi(\xi)}{\partial y} + \partial_y \right]. \quad (10)$$

In the present work, we first take the rapidity-space diffusion tensor to be constant and diagonal, but shall later also consider a rapidity dependence of the diffusion coefficient D_\parallel in longitudinal space.

It would be disadvantageous to formulate the model from the outset in (p_\perp, y) -space: an assumption of a diagonal diffusion tensor in this space of unlike variables is rather unconvincing. Of course, since collision data are usually represented as functions of transverse momenta p_\perp and rapidity y , or pseudorapidity η , solutions of our FPE will later be converted to (p_\perp, y) - or (p_\perp, η) -space, respectively.

In the rapidity-space FPE, the time parameter t and the diffusivity are the only dimensionful quantities. By introducing a dimensionless evolution parameter δ via $t =: t_0 + \Delta t \delta$, the equation can be rewritten as

$$\frac{\partial}{\partial \delta} f_\Xi(t_0 + \Delta t \delta) = \Delta t L_\Xi f_\Xi(t_0 + \Delta t \delta), \quad \delta > 0, \quad (11)$$

with the interaction timespan $\Delta t := t^* - t_0$. Here, t_0 represents the initial time, and solving the equation up to $\delta = 1$ corresponds to evolving it until the final time t^* . Due to the shape of the FPO, the diffusivity coefficients and interaction timespan can be combined to form the dimensionless products $D_\perp \Delta t$ and $D_\parallel \Delta t$, whose numerical values determine how close the final state is to the initial ($D_\perp \Delta t, D_\parallel \Delta t \ll 1$) or asymptotic state ($D_\perp \Delta t, D_\parallel \Delta t \gg 1$). This corresponds to an intrinsic symmetry of diffusive systems: changing the interaction timespan while reciprocally adjusting drift and diffusivity leaves the final state unchanged. Mathematically, this is related to a self-similarity of the standard Wiener process $W(t)$: for any constant $\alpha > 0$, the process $\widetilde{W}(t) := \frac{1}{\sqrt{\alpha}} W(\alpha t)$ is also a standard Wiener process. We shall later use Eq. (11) for the numerical solution of the problem.

The connection of the probability density functions of a stochastic model to the distribution of different particle species in phase space is made by scaling with the total particle number N . In relativistic heavy-ion collisions, energy and particle-number densities are highly inhomogeneous in position space, so it can be expected that particle dynamics depends on spatial coordinates as well – whereas the subprocess in momentum space used here assumes that its coefficient functions do not depend on positional coordinates. To address this issue, in previous applications of the model, the system has been split into multiple disconnected subsystems (*sources*) [30,31]

$$\frac{d^n N}{d^n q}(\mathbf{q}) = \sum_a N_a f_{Q_a}(\mathbf{q}, t^*), \quad \text{with} \quad \sum_a N_a = N, \quad (12)$$

for which different initial and asymptotic states can be chosen, thereby decoupling their time evolutions with independent FPOs. Conceptually, each source occupies a distinct region in phase space, with overlap between the different regions deemed negligible. Although this approach has been proven successful [31,2], its implementation has revealed itself particularly challenging for the solution method based on the spectral eigenfunction decomposition of the FPO that we use in the present work. The reasons will be discussed in the next chapter, along with the nature and relative contribution of each source to particle thermalization at LHC energies. In the actual calculations, only a single source will be considered, with meaningful results obtained nonetheless.

2.1 Initial state

The initial particle distribution functions are derived from a QCD-inspired phenomenological framework based on gluon saturation in the deep-inelastic scattering of participant partons [32,33,34,35], which was already successfully used [17,18,19] in the context of baryon stopping, and which appears to be compatible with a recent analysis of initial-state signals in ALICE data [36].

Here, the key assumption is that the gluon density saturates below a characteristic momentum scale Q_s , so that the respective gluons form a color-glass condensate (CGC). For small values of the gluon Bjorken momentum fraction x , this scale can be parametrized as [37]

$$Q_s^2(x) = \sqrt[3]{A} Q_0^2 \left(\frac{x_0}{x}\right)^\lambda, \quad (13)$$

where the values $\lambda = 0.2$ and $\frac{4}{9} Q_0^2 x_0^\lambda = 0.09 \text{ GeV}^2$ are used to be consistent with Refs. [19,2]. These values can

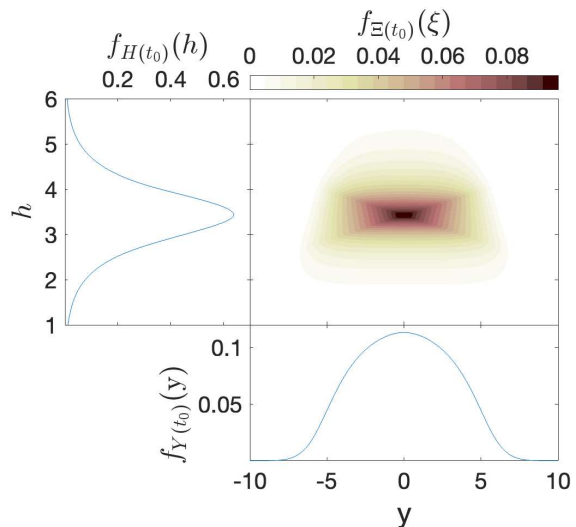


Fig. 1 Initial probability density function (PDF) of the central gluon-gluon pion source, Eq. (15), for a $\sqrt{s_{NN}} = 2.76$ TeV Pb-Pb collision. The joint distribution is shown in the central panel as a contour plot, with the color scale on the top. The left and the bottom panels contain the marginal PDFs in transverse and longitudinal rapidity, respectively.

be compared with literature results, where $\lambda \approx 0.288$ and $Q_0^2 x_0^\lambda \approx 0.097 \text{ GeV}^2$ were determined in a fit to deep-inelastic scattering e-p data from HERA [37].

The interaction of the participating nucleons is assumed to be mediated by quark-antiquark pairs (dipoles) emitted by the confined partons, which then inelastically scatter off the partons of the oppositely moving nucleus. Subsequent recombination of the quarks and gluons results in the production of new hadrons, which are emitted from the nuclear fragments. From the mass m and rapidities (h, y) of the produced hadron, the Bjorken momentum fractions x_\pm of the two generating partons contained in the forward (+) and backward (−) moving nucleon can be reconstructed from kinetic considerations to be

$$x_\pm \approx \frac{m \cos(h) \exp(\pm y)}{2m_N \sinh(y_b)}, \quad (14)$$

with y_b the beam rapidity and m_N the nucleon mass. Eq. (14) is an approximation obtained by simply imposing energy and longitudinal momentum conservation, ignoring the small initial transverse motion of the nucleons in the center-of-momentum frame, as well as the comparatively small parton masses contribution to the energy and any additional valence quarks that may be needed.

At low Bjorken x , the nucleon momentum is mostly carried by gluons, while valence quarks prevail at high x . For two interacting partons, this results in four dominant interaction processes that constitute the discon-

nected sources present in Eq. (12): gluon-gluon (gg), gluon-valence quark (gq), valence quark-gluon (qg) and quark-quark (qq) interactions. In this work, we consider only gluon-gluon scattering which predominantly yields hadronic particle-antiparticle pairs with low to intermediate y . Their initial PDF can be approximated by [38]

$$f_{\Xi(t_0)}(\xi) \approx C_{\text{gg}} \sinh(h) \cosh(h) \times \prod_{i \in \{+, -\}} x_i \frac{G(x_i; m \sinh(h))}{\sinh(h)^2} \Theta(1 - x_i), \quad (15)$$

where G is the simplified gluon structure function

$$xG(x; Q) \propto (1 - x)^4 \min(Q^2, Q_s^2(x)), \quad (16)$$

and C_{gg} is a numerically determined normalization constant. Eq. (15) is completely symmetric under the exchange of the forward- and backward-going gluon, and depends on the rapidity y through $x_{\pm}(y, h)$. The Heaviside theta functions are needed to ensure the validity of the Bjorken momentum fraction of the gluons since Eq. (14) is physically valid only for $x \leq 1$. An illustration of Eq. (15) for a Pb-Pb collision at $\sqrt{s_{\text{NN}}} = 2.76$ TeV is shown in Fig. (1).

The hadron yield of the qq process is expected to be small compared to the other three and can thus be safely neglected, but one should not in principle ignore the contribution given by the interactions of gluons and valence quarks. These two *fragmentation* sources produce particles at higher rapidities than the central source, and while essential to describe baryon stopping [19], their relevance in particle thermalization for central collisions at LHC energies is found to be small [2]. In the present work, these sources are not included because of the difficulty to account for their time evolution with the employed spectral eigenfunction decomposition, as we shall illustrate in detail when considering later the convergence properties of our algebraic solution method.

2.2 Asymptotic state

If the particles produced in a relativistic heavy-ion collision maintained their interactions for an extended period without ceasing due to the physical freeze-out, it is expected that the system would undergo thermalization and reach a stationary state in momentum space. In contrast, in position space, due to the absence of spatial confinement, the system cannot reach a stationary state that is independent of its initial configuration, and it would continue to expand into the surrounding vacuum leading to a finite collective particle flow [39]. Consequently, the equilibrium state in momentum space of

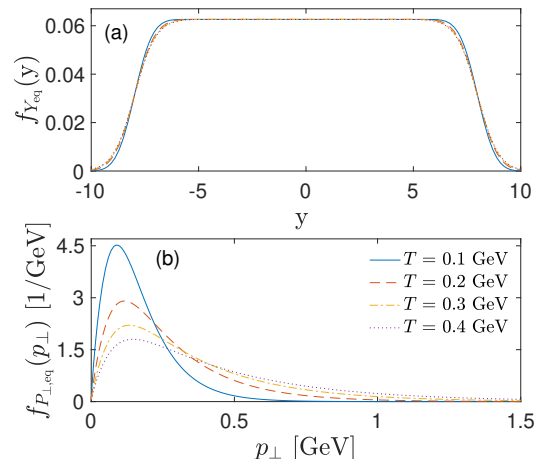


Fig. 2 Asymptotic marginal PDFs for pion production in a central $\sqrt{s_{\text{NN}}} = 2.76$ TeV Pb-Pb collision for different temperatures T as function of (a) y and (b) p_{\perp} . Other parameters as in Table 1. Considering another particle species has the same effect as changing T for $f_{Y_{\text{eq}}}$, while greater masses move the peak of $f_{P_{\perp, \text{eq}}}$ at higher p_{\perp} .

any produced charged hadron can be modeled by a generalized Maxwell-Jüttner distribution for an expanding thermal reservoir

$$f_{\mathcal{P}_{\text{th}}}(\mathbf{p}) := \frac{C_{\text{th}}}{V} \int_{\Sigma} \frac{d\sigma_{\mu} p^{\mu}}{p^0} \exp\left(\frac{m - u_{\nu} p^{\nu}}{T}\right), \quad (17)$$

where $\Sigma \subseteq \mathbb{R}^{1,3}$ denotes the (3+1)-dimensional space-time hypersurface containing the reservoir and u_{ν} its proper collective-flow velocity, which may depend on the position $\sigma \in \Sigma$. The total volume of the expanding reservoir is defined as $V := \int_{\Sigma} d\sigma_{\mu} u^{\mu}$, and C_{th} is a normalization constant independent of Σ and u_{ν} that can be computed analytically to be

$$C_{\text{th}} = \frac{\kappa}{4\pi m^3 \exp(\kappa) K_2(\kappa)}, \quad (18)$$

in terms of the dimensionless ratio between mass and temperature $\kappa := m/T$ and the modified Bessel function K_a of the second type and order a .

The simplest concrete implementation of Eq. (17) is obtained by considering a non-expanding reservoir at rest, $u^{\nu} = (1, 0, 0, 0)$, that leads to the original Maxwell-Jüttner distribution

$$f_{\mathcal{P}_{\text{M,J}}}(\mathbf{p}) = C_{\text{th}} \exp\left(\frac{m - p^0}{T}\right), \quad (19a)$$

which is the relativistic generalization of the Maxwell-Boltzmann distribution proposed by Jüttner [40] in 1911. It is useful to look at the marginal PDFs of Eq. (19a)

in transverse and longitudinal rapidity space:

$$f_{H_{MJ}}(h) = \frac{\kappa}{K_2(\kappa)} \sinh(h) \cosh(h)^2 K_1(\kappa \cosh(h)), \quad (19b)$$

$$f_{Y_{MJ}}(y) = \frac{1}{2K_2(\kappa)} \left[1 + \frac{2}{\kappa \cosh(y)} + \frac{2}{(\kappa \cosh(y))^2} \right] \times \exp(-\kappa \cosh(y)). \quad (19c)$$

The full width at half maximum (FWHM) of the marginal rapidity distribution ΔY_{MJ} is bounded from above by its value at the infinite-temperature limit of $2 \cosh^{-1}(\sqrt{2})$ for every finite T . This fact, which holds for a purely spherical flow as well, is in contrast with experimentally observed charged-hadron distributions at LHC energies that have a broader spectrum.

This problem has been addressed by considering a cylindrical-shaped expansion that spreads faster in the longitudinal than in the transverse direction: a Bjorken flow [41] in the longitudinal direction with maximum flow rapidity y_s [42]

$$f_{\Xi_{Bj}}(\xi) = \frac{1}{2y_s} \int_{-y_s}^{y_s} f_{\Xi_{\perp}}(h, y - \zeta) d\zeta \quad (20)$$

on top of a transverse expansion $f_{\Xi_{\perp}}$. To account for the well-known fact that conventional thermal models fail to describe the transverse high-momentum tails of charged-hadron data [43,44], following a phenomenological model proposed by Hagedorn [44], we have replaced [2] the exponential in Eq. (17) by

$$\widetilde{\exp}(x; n) := \left(1 + \frac{x}{n} \right)^n, \quad \text{with } x = \frac{m - u_{\nu} p^{\nu}}{T}. \quad (21)$$

For small values of its argument, that is for $|x/n| \ll 1$, Eq. (21) behaves as an exponential function: $\widetilde{\exp} \sim \exp(x)$, whereas for $|x/n| \gg 1$, it scales as a power law: $\widetilde{\exp} \sim (x/n)^n$. This behavior captures the observed transition from a thermal distribution at low transverse momentum to a power-law decay (Pareto law) in the p_{\perp} tail of charged-hadron spectra, which is often attributed to the increasing importance of hard processes in this regime that are not covered by thermal physics. However, when comparing to experimental data with $p_{\perp} > 2$ GeV, it turns out that the value of $n = -8$, adopted in our Ref. [2] for $p_{\perp} \leq 2$ GeV following an analysis of ALICE p-p data [45], overestimates the particle yield at high- p_{\perp} . Different values of n improve the situation in the momentum tail, but only at the expense of a decreased accuracy in describing the low- p_{\perp} region.

The agreement with high- p_{\perp} data can be improved by considering for the asymptotic distribution an approach by Bonasera et al. [46], who have employed a generalized Fokker-Plank solution (GFPS) to describe

charged-particle transverse distributions at various LHC energies and centralities according to

$$f_{E_{TGFPs}}(E_{\perp}) = C_{GFPS} \left[1 + \left(\frac{E_{\perp}}{b} \right)^d \right]^{-c} \times \exp \left(-\frac{b}{\hat{T}} \arctan \frac{E_{\perp}}{b} \right), \quad (22)$$

where $E_{\perp} := \sqrt{p_{\perp}^2 + m^2} - m$; c, d are parameters, and \hat{T} is a temperature-like quantity that may differ from the equilibrium temperature T because Eq. (22) is not a thermal distribution. When $p_{\perp} \ll 1$ or $\frac{E_{\perp}}{\hat{T}} \ll 1$, f_{GFPS} behaves as $e^{-E_{\perp}/\hat{T}}$, while in the high-momentum limit it follows the power law p_{\perp}^{-cd} . Motivated by the success of Eq. (22) in describing the transverse spectra across multiple orders of magnitude, we model the asymptotic distribution of the central gluon-gluon source as

$$f_{\Xi_{eq}}(\xi) = f_{H_{GFPS}}(h) \frac{1}{2y_s} \int_{-y_s}^{y_s} f_{Y_{MJ}}(y - \zeta) d\zeta, \quad (23)$$

which is the product of Eq. (22) expressed in terms of the transverse rapidity h , including the determinant of the transformation, and a Bjorken flow in y based on the marginal Maxwell-Jüttner distribution Eq. (19). The marginal distributions of Eq. (23) in y and p_{\perp} for pion production are plotted in Fig. 2.

When considering the marginal rapidity distribution, $f_{Y_{eq}}(y)$ is only slightly different from $f_{Y_{Bj}}(y)$ obtained by marginalizing Eq. (20), but it improves the modeling of the transition from exponential to power-law decay in the transverse direction. In addition, the product form $f_{\Xi_{eq}} = f_{H_{eq}} f_{Y_{eq}}$ greatly speeds up the numerical solution. While in general such a form may not describe precisely the expected two-dimensional asymptotic state in the whole phase-space, this approximation is good enough for low-to-intermediate rapidity, where $f_{Y_{eq}}$ is essentially constant, as seen in Fig. 2 (a). Since no experimental data are available beyond this region, it is difficult to speculate where this approach starts to fail. In the next section, we proceed to the spectral solution method of the FPE.

3 Spectral method of solution

Spectral methods represent a powerful and versatile class of numerical techniques employed to solve partial differential and integral equations. Unlike traditional finite difference or finite element methods, the idea at the foundations of spectral methods is expressing solutions in terms of basis functions with global support. When applied to a smooth problem on a simple domain, spectral methods can achieve exceptional accuracy compared to other numerical methods, and the

convergence is usually exponential in the number of basis functions or evaluation points [47, 48].

We first discuss the use of non-classical orthogonal polynomials to efficiently construct a spectral representation of the FPO. Using such a basis set, it is possible to implement a representation of the one-dimensional operator that does not require an explicit calculation of the drift coefficient via the FDR, while for the higher-dimensional case, the equivalence between the Fokker-Planck and a Schrödinger equation can be exploited.

To construct a non-classical basis set, consider the polynomials $\{P_m\}$ orthonormal with respect to some weight function w on $(a, b) \in \mathbb{R}$, that is,

$$\int_a^b w(x) P_m(x) P_\perp(x) dx = \delta_{m\perp}. \quad (24)$$

The polynomials form a basis set and satisfy the general three-term recurrence relation [49]

$$x P_m(x) = \sqrt{\beta_m} P_{m-1}(x) + \alpha_m P_m(x) + \sqrt{\beta_{m+1}} P_{m+1}(x), \quad (25)$$

where the coefficients α_m and β_m can be determined with the Stieltjes procedure [50].

3.1 Spectral representation of the 1D FPO

The one-dimensional FPO can be converted into a Hermitian form by multiplying it with e^Φ , that is, by dividing it by the stationary solution $f_{X_{\text{eq}}}$ ¹. Writing the general time-dependent solution $f_X(x, t)$ as the product of the stationary solution and an auxiliary function $g_X(x, t)$

$$f_X(x, t) := f_{X_{\text{eq}}}(x) g_X(x, t), \quad (26)$$

the FPE for the function g_X becomes

$$\begin{aligned} \frac{\partial g_X}{\partial t} &= \frac{1}{f_{X_{\text{eq}}}} \frac{\partial}{\partial x} \left[D_X f_{X_{\text{eq}}} \frac{\partial g_X}{\partial x} \right] \\ &= \mu_X \frac{\partial g_X}{\partial x} + D_X \frac{\partial^2 g_X}{\partial x^2} = G_X g_X, \end{aligned} \quad (27)$$

where G_X is self-adjoint with respect to the equilibrium solution as a weight function

$$\begin{aligned} \langle \phi_1 | G_X | \phi_2 \rangle &= \int f_{X_{\text{eq}}} \phi_1 G_X \phi_2 dx \\ &= \int f_{X_{\text{eq}}} \phi_2 G_X \phi_1 dx \\ &= \langle \phi_2 | G_X | \phi_1 \rangle, \end{aligned} \quad (28)$$

¹ $f_{X_{\text{eq}}}$ is assumed to be normalized, such that all normalization factors are ignored in this section.

provided the zero flux boundaries condition

$$\int_{\partial V} f_{X_{\text{eq}}} D_X \frac{\partial g}{\partial x} dx = 0. \quad (29)$$

To construct an efficient spectral representation of the operator G_X , a basis of non-classical polynomials $\{P_m\}$ orthogonal w.r.t. the stationary solution of the FPE can be employed. Such a basis satisfies Eq. (24) with $w = f_{X_{\text{eq}}}$, and has the advantage that it is automatically adapted to the specific problem. In addition, knowing that the first eigenfunction of the FPO is the equilibrium distribution and that the successive eigenfunctions are orthogonal to it, a basis set satisfying the same orthogonality relations is special compared to other polynomial sets. The spectral representation of G_X in this basis is [51, 52, 53]

$$\begin{aligned} G_X^{\text{ml}} &= \int f_{X_{\text{eq}}} P_m G_X P_\perp dx \\ &= \int f_{X_{\text{eq}}} P_m \frac{1}{f_{X_{\text{eq}}}} \frac{d}{dx} \left[f_{X_{\text{eq}}} D_X \frac{dP_\perp}{dx} \right] dx. \end{aligned} \quad (30)$$

Integrating by parts and making use of the orthogonality of the basis set w.r.t. the stationary solution, the expression simplifies to

$$G_X^{\text{ml}} = \int f_{X_{\text{eq}}} D_X P'_m P'_\perp dx, \quad (31)$$

where natural boundary conditions were assumed. This representation is particularly convenient because it only requires polynomial derivatives that can be carried out analytically. Since the drift function does not explicitly appear in the expression, if one already knows the stationary solution and the form of the diffusion coefficient, the use of the FDR is not even necessary. The eigenvalues λ_m and eigenfunctions ψ_m of the operator G_X can be estimated by diagonalization of the $(M+1) \times (M+1)$ symmetric matrix G_X^{ml} , where $M+1$ is the dimension of the orthonormal basis set $\{P_m\}$. It was shown numerically that the coefficients of the expansion of ψ_n in the $\{P_m\}$ basis set are linear variational parameters. The variational theorem then guarantees that this method provides an upper bound to the eigenvalues for each M and converges from above.

The FPO L_X and G_X share the same eigenvalues, and are connected through

$$G_X = e^\Phi L_X e^{-\Phi}. \quad (32)$$

The time-dependent solution of the FPE can be then approximated by

$$f_X(x, t) \approx f_{X_{\text{eq}}}(x) \sum_{m=0}^M c_m \psi_m(x) e^{-\lambda_m(t-t_0)}, \quad (33)$$

where the coefficients c_m are determined from the initial condition by

$$c_m = \int f_X(x, t_0) \psi_m(x) dx. \quad (34)$$

The goodness of Eq. (33) in approximating $f_{X(t)}$ depends of course on the convergence of the eigenvalues and eigenfunctions of the FPO, and on the convergence of the coefficients c_m to small values when approaching the M -th element.

3.2 Representation of the 2D Schrödinger operator

The stochastic process Eq. (5) is characterized by a two-dimensional FPO, for which the simple 1D representation described above cannot be employed. The equivalence between the FPE and a Schrödinger equation with a supersymmetric potential is a well-understood fact [54, 55], and it is useful to take advantage of the large class of solution methods of quantum mechanical problems. Finding a spectral solution of the FPO can then be reduced to the eigenvalue equation of a 2D Hamiltonian where the Schrödinger potential can be obtained from the drift and diffusion coefficient functions. An explicit transformation in the case of constant diagonal diffusion is given in Ref. [56].

Unfortunately, it is not generally possible to construct an orthonormal set of polynomials of two variables (x, y) w.r.t. some weight function $w(x, y)$, and two different basis sets have to be employed to construct a spectral representation [52]. In contrast to the one-dimensional representation Eq. (31), the explicit calculation of the drift coefficient and its derivative is necessary to obtain the Schrödinger potential. If μ_X is constructed from the FDR, that means carrying out second derivatives of the asymptotic PDF. As explained in Sect. 4, it will be sufficient to solve an effective 1D FPE for our case of interest, and we can then avoid the use of this 2D representation.

3.3 Convergence of the spectral expansion

We limit the discussion of the FPE spectral solution convergence to the marginal one-dimensional rapidity FPO

$$L_Y = D_{\parallel} \frac{\partial}{\partial y} \left[-\frac{\partial \ln f_{Y_{\text{eq}}}(y)}{\partial y} + \frac{\partial}{\partial y} \right], \quad (35)$$

which can be solved employing the representation Eq. (33) after the transformation to its Hermitean form G_Y . In Fig. 3, the extremely fast convergence of this solution scheme is shown when considering the FPO generated

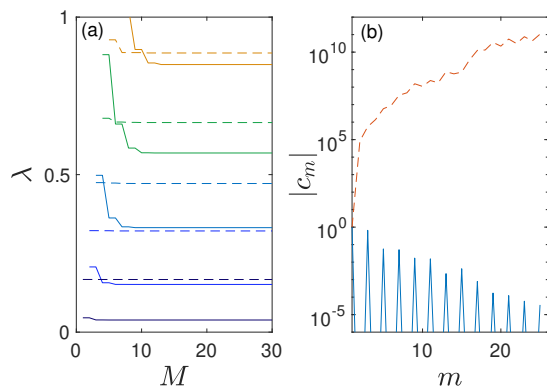


Fig. 3 Spectral convergence of the FPE for the central gluon-gluon (solid curves) and the fragmentation sources (dashed curves). (a) The first five positive eigenvalues of the adimensional marginal rapidity FPO are plotted against the orthogonal basis dimension M . The eigenvalues of the fragmentation FPO are scaled by 0.18 for better visualization. (b) Absolute value of the expansion coefficients c_m (logarithmic scale) calculated from the initial PDF of the central (solid) and forward (dashed) sources. $M = 25$.

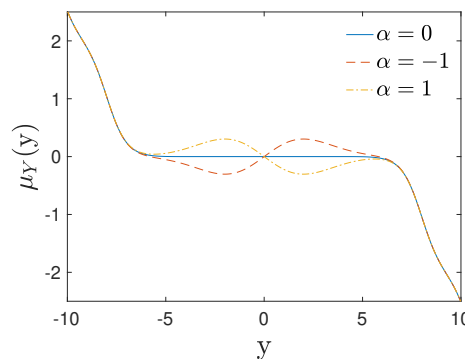


Fig. 4 Drift coefficient μ_Y for three different values of α . The $f_{Y_{\text{eq}}}$ in the FDR describe pion thermalization in $\sqrt{s_{\text{NN}}} = 2.76$ TeV Pb-Pb collisions. Parameters as in Table 1, except for $D_{\parallel} \Delta t = 1$. The solid blue line, corresponding to $\alpha = 0$, represents the case of a constant diffusion. The dashed red line and the dot-dashed yellow line are calculated for $\alpha = -1$ and $\alpha = 1$, respectively.

by the marginal rapidity central gluon-gluon source asymptotic PDF for hadron thermalization in a Pb-Pb collision at $\sqrt{s_{\text{NN}}} = 2.76$ TeV with constant diffusion D_{\parallel} . As inferred from Fig. 3 (a), using an orthogonal basis of dimension $M = 15$ is already sufficient to obtain a good convergence of the first five positive eigenvalues. Given this fact, for the subsequent results presented in this work, a basis dimension of $M = 25$ is employed, which is deemed sufficient for obtaining a satisfactory precision of the relevant FPE solution. Panel (b) shows on a logarithmic vertical scale the exponential approach to zero of the expansion coefficients c_m , calculated using Eq. (34) with the initial PDF of the central gg source Eq. (15) and the eigenfunctions of G_Y calculated with

$M = 25$. The values of the coefficients corresponding to odd eigenfunctions are zero up to machine precision, as expected by the y -parity of both the FPO and the initial condition.

In contrast to the success of this spectral solution scheme in solving the central-source FPE, Fig. 3 also illustrates its failure when applied to the forward quark-gluon and backward gluon-quark fragmentation sources. In panel (a), the dashed lines show that the convergence of the eigenvalue is even faster than for the gg source, but from panel (b) it can be observed that the absolute values of c_m explode for the higher eigenfunctions, and therefore a good approximation of the initial state with a finite-dimensional polynomial basis orthogonal to $f_{Y_{eq}}$ cannot be reached. To understand why that is the case, the fragmentation equilibrium and initial states rapidity dependence have to be analyzed. Similarly to the central fireball, the marginal longitudinal asymptotic state is given by a y -symmetric Bjorken flow Eq. (20) for both the qg and qg sources. The (backward)forward source initial PDF is again derived from the DIS-CGC-formalism, and is peaked around $(-)y_b$. It turns out that the forward qg marginal rapidity asymptotic and initial PDF – as employed in Ref. [2] – occupy two almost disconnected regions in rapidity space. At the peak of $f_Y(t_0)$, the extremely fast decay of $f_{Y_{eq}}$ has already reached the machine noise level. While it is theoretically true that an infinite-dimensional orthogonal basis set defined by Eq. (24) on \mathbb{R} is complete, and can then approximate any continuous function, in practice one can only generate a finite set. Consequently, the method is not suited in practice to calculate the time evolution of the fragmentation sources.

4 Comparison with LHC data

For $^{208}\text{Pb-Pb}$ collisions at LHC energies, the only available particle-production data in the rapidity region up to $y = 5$ are for unidentified charged hadrons h^\pm , because no suitable spectrometer for hadron identification has been installed yet at $|y| > 2$. Consequently, the measured distributions are given in terms of the coordinates (p_\perp, η) , where η is the pseudorapidity

$$\eta := \text{artanh}\left(\frac{p^3}{|\mathbf{p}|}\right) = \text{arsinh}\left(\sqrt{1 + \left(\frac{m}{p_\perp}\right)^2} \sinh(y)\right), \quad (36a)$$

and the Jacobian matrix for the transformation from (p_\perp, y) to (p_\perp, η) space is given by

$$\frac{\partial(p_\perp, \eta)}{\partial(p_\perp, y)} = \begin{pmatrix} 1 & 0 \\ -\frac{\tanh(\eta)}{p_\perp [1 + (\frac{m}{p_\perp})^2]} & \sqrt{1 + \left(\frac{m}{p_\perp \cosh(\eta)}\right)^2} \end{pmatrix}. \quad (36b)$$

The measurement of $\eta = -\ln[\tan(\theta/2)]$ requires only the knowledge of the scattering angle θ , which is available without particle identification. The pseudorapidity agrees with y for $|\mathbf{p}| \gg m$. The charged-particle yield is mainly composed of pions, followed by kaons and (anti)protons, with the measured abundance fractions of approximately 83%, 13%, and 4%, respectively, in 2.76 TeV Pb-Pb [57,58].

Comparison with data from ALICE [20,21,22] and ATLAS [23] of Pb-Pb collisions with $\sqrt{s_{NN}} = 2.76$ and 5.02 TeV is performed by evolving the initial PDFs of the three hadron species separately with a common value of $D_\perp \Delta t$ in the (h, y) coordinate space. Then, the obtained PDFs are transformed to the (p_\perp, η) space with the appropriate determinant, multiplied by the total number of particles N , and finally summed according to the above percentages. While in principle every particle species could have an independent set of parameters, the lack of identified hadron spectra would make the then abundant parameter space difficult to fit meaningfully to the available data. For this reason, the initial and final PDFs for pions, kaons, and protons are assumed to differ only by the respective particle masses, $m_\pi = 139.6$ MeV, $m_K = 493.7$ MeV, and $m_p = 938.3$ MeV, and share the rest of the free parameters.

The parameter space can be additionally reduced by adopting two results from our Ref. [2]. There, we have identified the maximum Bjorken flow rapidity y_s for the central gluon-gluon source with the beam rapidity y_b , and it has been verified that the equilibration in the transverse direction happens much faster than in the longitudinal one, corresponding to $D_\perp \Delta t \gg D_\parallel \Delta t$. While this is not physically surprising, as thermal models with modified high-momentum tails are known to well describe transverse charged-hadrons spectra, it affects negatively the precision and speed of the numerical solution of the FPE. Following the same approach as in Ref. [2], the problem is circumvented by taking the limit $D_\perp \Delta t \rightarrow \infty$, which in practice means assuming an almost instantaneous thermalization in the transverse direction. Hence, the problem reduces to solving only the marginal one-dimensional longitudinal FPE

$$\frac{\partial f_Y}{\partial t} = \left[-\frac{\partial}{\partial y} \mu_Y + \frac{\partial^2}{\partial y^2} D_Y \right] f_Y, \quad (37)$$

$\sqrt{s_{\text{NN}}} \text{ (TeV)}$	y_b	$N \times 10^{-4}$	$D_{\parallel} \Delta t$	α	$\hat{T} \text{ (MeV)}$	$b \text{ (GeV)}$	cd	χ^2/ndf
2.76	7.99	1.713(8)	0.98(9)	-1	486(4)	9.4(5)	0.30(2)	134/193
5.02	8.58	2.182(8)	1.055*	-1	624(7)	22(4)	2.8(2)	28/66
5.36	8.65	2.237*	1.063*	-1*	639*	24*	3.06*	-

Table 1 Model parameters for central Pb-Pb collisions determined in χ^2 minimizations to ALICE and ATLAS data, and extrapolation to $\sqrt{s_{\text{NN}}} = 5.36$ TeV. Numbers in brackets indicate the estimated uncertainty of the preceding digit; see text for details, and for the physical meaning of the temperature-like parameter \hat{T} . Numbers marked with * are extrapolated as explained in the text. The value of c is fixed to 5.

which can be done with the efficient spectral representation Eq. (31). The two-dimensional joint distribution can then be reconstructed by

$$\begin{aligned} f_{\Xi}(\xi, t^*) &\approx f_Y(y, t^*) f_{H_{\text{eq}}|Y_{\text{eq}}}(h|y) \\ &= \frac{f_Y(y, t^*)}{f_{Y_{\text{eq}}}(y)} f_{\Xi_{\text{eq}}}(\xi). \end{aligned} \quad (38)$$

Since the explicit use of the FDR is not necessary in this simplified case, and being motivated by the difficulty of a constant longitudinal diffusion coefficient to reproduce the midrapidity region encountered previously [2], it is straightforward to allow for a rapidity-dependent diffusion $D_Y(y)$. Imposing that D_Y is continuous, differentiable, positive $\forall y$ and respects the even symmetry of the system, a simple form is given by

$$D_Y(y) = D_{\perp}(1 + \alpha e^{-y^2/y_b}), \quad \alpha > -1, \quad (39)$$

where the denominator of the exponential is chosen to be y_b as it is the only fixed rapidity scale of the system, and treating it as a free parameter does not improve significantly the fit to the data. Since the solution obtained with a constant diffusion predicted a particle yield around $y = 0$ too low compared to the data, and because in that region the PDF is monotonically decreasing in the time evolution, it is expected that negative values of α should improve the modeling of hadron spectra, as will be shown by the fit to LHC data in the next subsection. The corresponding drift coefficient for positive and negative values of α is shown in Fig. 4.

Allowing for a rapidity-dependent diffusion, the free parameters of the model are $D_{\parallel} \Delta t$ and α that determine how much and how the solution approaches equilibration, the total number of particles N , and the parameters of the equilibrium PDFs. These are \hat{T} , b , and the exponents c and d . The fit to experimental data is based on a least- χ^2 determination. For every data point, the calculated PDF is integrated in the respective coordinate bin, and the result is subtracted from the experimental value and divided by the total uncertainties, statistic and systematic. These normalized residuals are squared and summed over all available data at each collision energy, and the resulting total χ^2 is minimized. Since the aim of the present work is to describe particle production in relativistic heavy-ion collision with

a non-equilibrium statistical model, comparison with data is carried out only in the $p_{\perp} \leq 4$ GeV region, outside which hard partonic interactions are expected to dominate over statistical effects. At high transverse momentum, a non-equilibrium statistical description such as the one employed in this work cannot be expected to hold, and perturbative QCD approaches as in Refs. [59, 60, 61] have to be applied. The minimization process is carried out with the MATLAB routine `fminsearch.m`, based on the Nelder-Mead simplex algorithm [62]. Uncertainties of the parameter vector θ are estimated with the square root of the covariance matrix diagonal, which is obtained by inverting the Hessian of $\chi^2(\theta)$. The latter is calculated numerically with the MATLAB suite DERIVEST [63].

4.1 Central $\sqrt{s_{\text{NN}}} = 2.76$ TeV Pb-Pb

The results of the parameter optimization for both LHC energies are shown in Table 1. While the transverse thermalization is almost instantaneous, the system remains very far from equilibrium in the longitudinal direction, as indicated by the relatively small values of $D_{\parallel} \Delta t$. The χ^2 optimization reaches the lower bound of $\alpha = -1$ for both $\sqrt{s_{\text{NN}}} = 2.76$ TeV and 5.02 TeV, corresponding to an almost vanishing equilibration at $y = 0$. As already argued in Ref. [46], it was verified that the parameters describing the transverse FPE solution are highly correlated. In particular, only the value of the product cd is relevant when stopping the fit at $p_{\perp} = 4$ GeV, and the degrees of freedom of the model were then reduced from seven to six. The high values of the parameter \hat{T} introduced in Ref. [46] are due to the fact that – different from the temperatures determined in Ref. [2] – it should not be identified with the physical temperature of the system, because the GFPS is not a (modified) thermal distribution.

For $\sqrt{s_{\text{NN}}} = 2.76$ TeV, the ALICE data set [20] contains measurements of the marginal pseudorapidity PDF in the $-5 \leq \eta \leq 5.5$ window. The comparison of our model results with the data is presented in Fig. 5. In the top panel (a), the total particle yield as a function of pseudorapidity η is shown as a solid blue curve, along with the individual contributions of pions, kaons, and

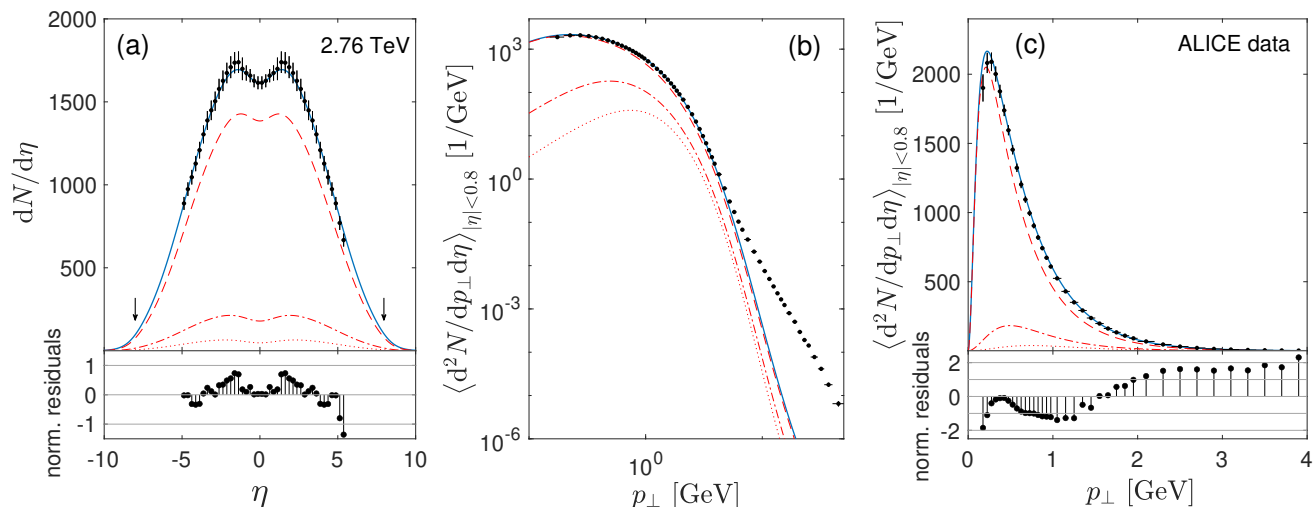


Fig. 5 (a) Comparison of the calculated marginal pseudorapidity charged-hadrons number density function $dN/d\eta$ of central $\sqrt{s_{NN}} = 2.76$ TeV Pb-Pb collisions to 0-5% ALICE data [20]. In the top panel, the solid blue curve indicates the total calculated particle yield, while the red dashed, dot-dashed, and dotted lines are the contributions of pions, kaons, and (anti)protons, respectively. The black dots are the experimental data points, with the vertical error bars including statistic and systematic error. The bins are smaller than the symbol size, and the black arrows mark the beam rapidity. The bottom panel shows the normalized residuals, as defined in the text, for every bin. (b) Comparison of the calculated joint produced charged-hadron spectrum $d^2N/d\eta dp_\perp$ to 0-5% ALICE data [22] in $\sqrt{s_{NN}} = 2.76$ TeV Pb-Pb central collisions, averaged over the $|\eta| < 0.8$ slice and plotted against p_\perp on a log-log scale. The four curves represent the same quantities as in (a). Horizontal bars indicate the bin size, and experimental error bars are smaller than the symbols. See text for the deviation beyond $p_\perp = 4$ GeV. (c) Same as in (b), but restricted to the interval $p_\perp < 4$ GeV and on a linear scale. Normalized residuals are shown in the bottom panel.

protons as red dashed, dot-dashed, and dotted lines. As can be inferred by the normalized residuals shown in the bottom panel, the model describes the pseudorapidity spectrum very well, with only the rightmost data point having an error exceeding 1σ . In particular, allowing for a rapidity-dependent D_Y produces a considerably better agreement with the data near the midrapidity dip compared to our previous results [2], where, due to the assumption of a constant diagonal diffusion, the particle yield at $y = \eta = 0$ was found to be too low. In Figs. 5 (b) and (c), the model predictions are compared with transverse-momentum data from ALICE [22], obtained by averaging over a $|\eta| \leq 0.8$ pseudorapidity slice. Fig. 5 (b) shows the whole experimentally available transverse momentum range up to $p_\perp = 50$ GeV in a log-log scale, with the total particle yield and the single species contributions represented as in Fig. 5 (a). The model prediction clearly deviates from the experimental data beyond $p_\perp = 4$ GeV – partly due to the fact that the subsequent transverse region was not included in the χ^2 minimization, but mainly because hard processes take over that are not covered in a nonequilibrium-statistical model. A closer look at the fitted region is given in Fig. 5 (c), where the comparison of the model to data is shown for $p_\perp \leq 4$ GeV using a linear scale, in the upper part. The correspond-

ing normalized residuals in the bottom panel indicate the deviations from the data.

The data set for 2.76 TeV Pb-Pb collisions shown in Fig. 6 is from the ATLAS experiment [23], and contains two-dimensional measurements of charged-hadron production in the window $0 \leq \eta \leq 2$ and $0.5 \leq p_\perp \leq 150$ GeV. In Fig. 6 (a) the calculated particle-number density function $d^2N/d\eta dp_\perp$ is shown as a two-dimensional contour plot with the logarithmic color scale on the right, and the normalized residuals are represented as superimposed rectangular bins with the linear color scale on top. The lower figure 6 (b) presents the same results, but plotted p_\perp -binwise against pseudorapidity, with each curve in η obtained by averaging the calculated differential yield over a p_\perp bin. The model gives an overall good description of the data, with the exception of the outer pseudorapidity region $1.5 \leq \eta \leq 2$, where the experimental measurements strongly deviate from the prediction, with a discrepancy of more than 2.5σ for the two outest bins. The apparent increase of the data around $\eta \simeq 2$ in the low- p_\perp bins cannot be accurately described with the assumption of a diagonal diffusivity, nor is it an effect of the Jacobian transformation from the (h, y) coordinate space. A more complex model would probably be needed to address this feature, unless it is due to an underestimate of the sys-

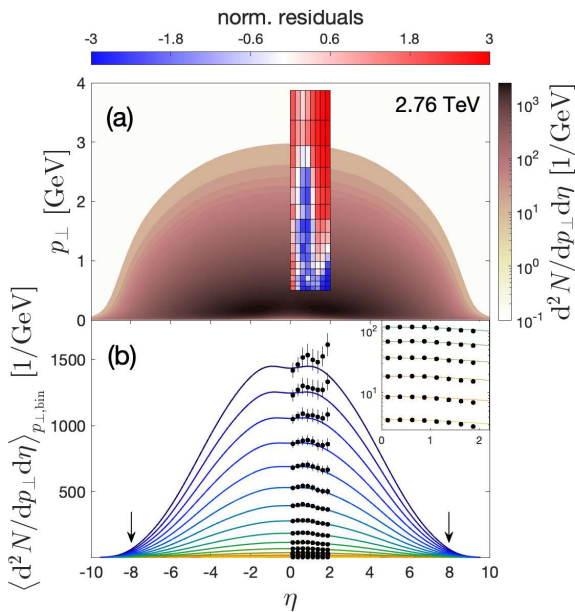


Fig. 6 (a) Joint two-dimensional spectrum of produced charged hadrons in $\sqrt{s_{\text{NN}}} = 2.76$ TeV Pb-Pb central collisions, compared to 0-5% ATLAS data [23]. The logarithmic color scale on the right refers to the calculated value of $d^2N/d\eta dp_{\perp}$, and the linear color scale at the top refers to the normalized residuals – data minus model prediction divided by total uncertainty – represented as rectangles the size of the corresponding experimental bin. (b) Same joint spectrum, but averaged over experimental p_{\perp} bins from $p_{\perp} = 0.5$ GeV (top curve) to $p_{\perp} = 3.87$ GeV (bottom curve) and plotted against positive η . The insert shows in detail the six lowest curves, from $p_{\perp} = 1.7$ GeV to $p_{\perp} = 3.87$ GeV, on a vertical logarithmic scale. Vertical and horizontal bars indicate the total uncertainties and the bin sizes in the η direction. The black arrows mark the beam rapidity.

tematic experimental error – especially when comparing to the ALICE marginal pseudorapidity data [20, 21] that show a much smoother trend at both, 2.76 and 5.02 TeV.

4.2 Central $\sqrt{s_{\text{NN}}} = 5.02$ TeV Pb-Pb

The calculated marginal pseudorapidity distribution for central Pb-Pb collision at $\sqrt{s_{\text{NN}}} = 5.02$ TeV is compared to ALICE data [21] covering the midrapidity window $-3.5 \leq \eta \leq 5$ in Fig. 7. As for the lower energy, the total hadron production $dN/d\eta$ is shown as a solid blue line, while the partial contributions of pions, kaons, and protons as red dashed, dot-dashed, and dotted lines in Fig. 7(a). Figures 7(b) and (c) present the model prediction in the transverse direction, obtained by averaging $d^2N/d\eta dp_{\perp}$ over the $|\eta| \leq 0.8$ pseudorapidity slice, in comparison with ALICE data [22]. Fig. 7(b) shows the whole measured p_{\perp} range plotted on a log-log scale, Fig. 7(c) analyzes only the $p_{\perp} \leq 4$ GeV fitted region

on a linear scale, and gives the associate normalized residuals. The spectrum is qualitatively similar to that at 2.76 TeV collision energy, apart from the expected higher total number of produced particles. Due to the change in slope of the 5.02 TeV $dN/d\eta$ ALICE data around $|\eta| \approx 4$ and the lack of a measured joint spectrum outside the midrapidity region, it proved difficult to obtain a reasonable fit result for the longitudinal diffusivity. The χ^2 minimization tried to compensate for these features in the data, resulting in an overfitted set of parameters predicting a high yield at intermediate-to-high rapidity. To address this problem that has already been encountered in Ref. [2], the 2.76 TeV result for $D_{\parallel}\Delta t$ is extrapolated to the higher energy by scaling it with the beam rapidity, based on the earlier finding [64] that the width of the marginal pseudorapidity distribution is in good approximation proportional to the logarithm of the respective center-of-mass energy. Despite having reduced the free parameters by fixing $D_{\parallel}\Delta t$, the model provides a satisfactory description of the experimentally measured spectrum in both the longitudinal and transverse directions.

4.3 Predictions for $\sqrt{s_{\text{NN}}} = 5.36$ TeV Pb-Pb

During Run 3 at the LHC, the ALICE experiment has collected data of Pb-Pb collisions at $\sqrt{s_{\text{NN}}} = 5.36$ TeV in 2023. Here we use the relativistic diffusion model to make a prediction of the charged-hadron spectra at this energy. Since no data are yet available, we extrapolate the free parameters of the model at $\sqrt{s_{\text{NN}}} = 5.36$ TeV from the lower energies. Regarding the approach to thermalization in the longitudinal direction, the value of $D_Y\Delta t$ can be obtained by scaling it with the beam rapidity, as already done for $\sqrt{s_{\text{NN}}} = 5.02$ TeV. Since α reaches the lower boundary of -1 for both of the lower energies, this is assumed to be the case at 5.36 TeV as well. As for the parameters describing the transverse spectrum as shown in Table 1, it is more difficult to infer a scaling with the energy. Apart from the condition $c = 5$ that is maintained, \hat{T} , b and d are also assumed to be proportional to y_b . For the total number of charged hadrons N , an investigation of the central and fragmentation sources in heavy-ion collisions at RHIC and LHC energies [16] found a phenomenological scaling of the gluon-gluon total charged-hadron yield with the cube of the beam rapidity. We use this dependence to predict N at 5.36 TeV. The extrapolated parameter set is given in Table 1. The resulting spectra in the longitudinal and transverse directions are shown in Fig. 8, with (a) the predicted joint spectrum $d^2N/d\eta dp_{\perp}$ of produced charged hadrons and (b) the

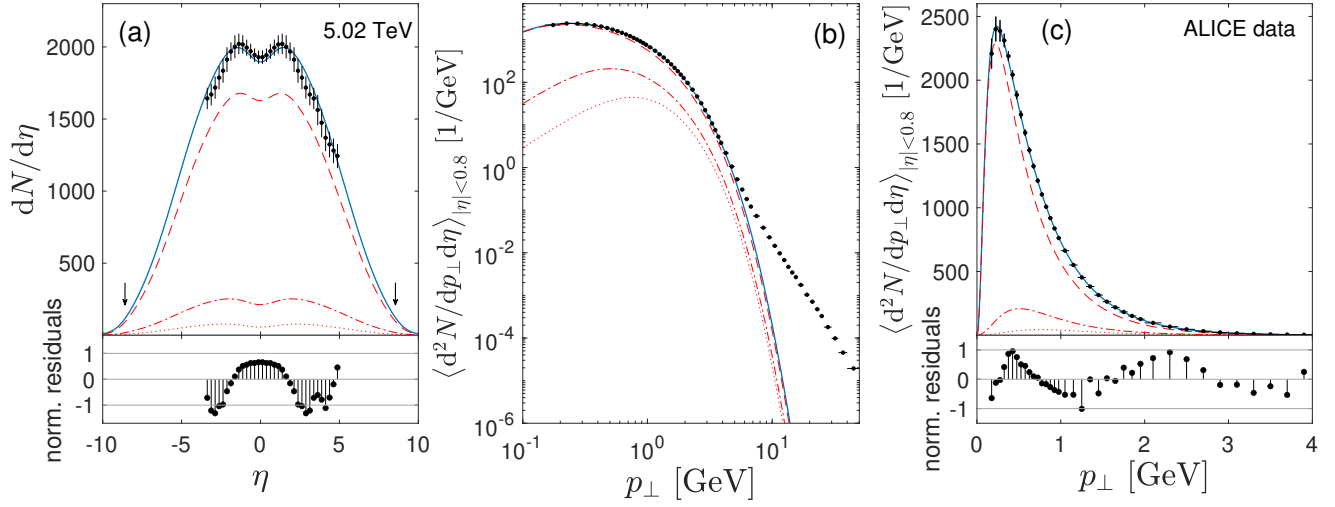


Fig. 7 (a) Comparison of the calculated marginal pseudorapidity charged-hadron number density distribution $dN/d\eta$ of central $\sqrt{s_{NN}} = 5.02$ TeV Pb-Pb collisions to 0-5% ALICE data [21] (black points). The top panel shows the total produced hadrons (solid curve) and the contribution of pions (dashed), kaons (dot-dashed), and (anti)protons (dotted). Horizontal bars represent the total experimental errors, the bins are smaller than the symbol size, and the black arrows mark the beam rapidity. The bottom panel shows the normalized residuals for every bin. (b) Comparison of the calculated joint produced charged-hadron spectrum $d^2N/d\eta dp_\perp$ to 0-5% ALICE data [22] in $\sqrt{s_{NN}} = 5.02$ TeV Pb-Pb central collisions, averaged over the $|\eta| < 0.8$ slice and plotted against p_\perp on a log-log scale. See text for deviation above 4 GeV. (c) Same as in (c), but restricted to the interval $p_\perp < 4$ GeV and on a linear scale. Normalized residuals are shown in the bottom panel.

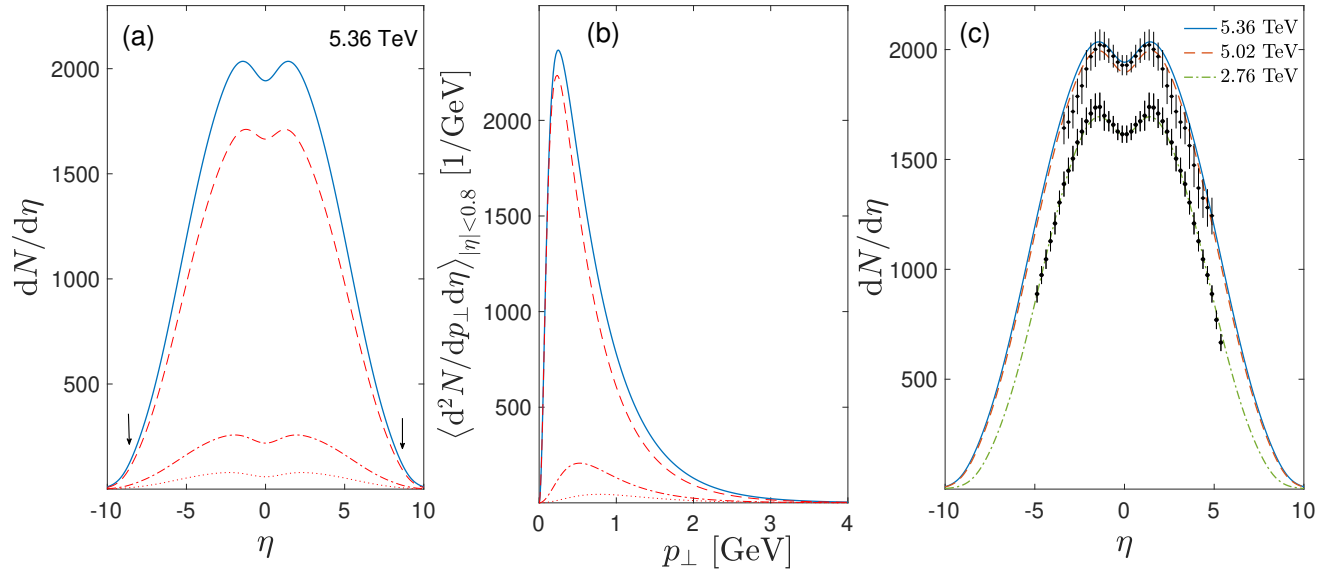


Fig. 8 (a) Predicted marginal pseudorapidity $dN/d\eta$ of produced charged hadrons in central $\sqrt{s_{NN}} = 5.36$ TeV Pb-Pb collisions. The curves are the total produced hadrons (solid) and the contribution of pions (dashed), kaons (dot-dashed), and (anti)protons (dotted). (b) Predicted joint spectrum $d^2N/d\eta dp_\perp$ of produced charged hadrons in $\sqrt{s_{NN}} = 5.36$ TeV Pb-Pb central collisions, averaged over the $|\eta| < 0.8$ slice and plotted against p_\perp . (c) Predicted marginal pseudorapidity $dN/d\eta$ of produced charged hadrons in central $\sqrt{s_{NN}} = 5.36$ TeV Pb-Pb collisions (solid curve) compared to the result at $\sqrt{s_{NN}} = 5.02$ TeV (dashed) and $\sqrt{s_{NN}} = 2.76$ TeV (dot-dashed), with ALICE data as in Figs. 5,7.

corresponding transverse-momentum distribution. According to Ref. [16], the particle yield at mid-rapidity is in good approximation

$$\left. \frac{dN}{d\eta} \right|_{\eta=0} \approx 1150 \left(\frac{s_{NN}}{s_0} \right)^{0.165}, \quad (40)$$

with $s_0 = 1 \text{ TeV}^2$. The predictions of this phenomenological law agree with the existing data at both LHC energies, but slightly deviate from the present model prediction of the 5.36 TeV longitudinal spectrum. In Fig 8 (c), the marginal pseudorapidity hadron yields of the relativistic diffusion model as calculated using the spectral solution method are shown for all three energies in comparison with the presently available ALICE data.

5 Conclusions

A spectral eigenfunction decomposition of the Fokker-Planck operator derived from a drift-diffusion model for partial thermalization of produced charged hadrons in relativistic heavy-ion collisions has been developed and implemented. The representation of the Fokker-Planck operator is based on a polynomial basis constructed with an orthonormality relation with respect to the stationary solution of the Fokker-Planck equation, which is the first eigenfunction of the associated differential operator. When considering the central fireball, which is the main source of particle production through gluon-gluon interactions at LHC energies, such a spectral method is successfully applied, and the convergence of the solution is shown to be very fast. It turns out to be difficult, however, to employ the same spectral representation to solve the FPE for the forward and backward fragmentation sources, because the overlap between initial and stationary distribution is very small.

The high accuracy of the spectral solution method allows to compare the calculated spectrum in a large transverse-momentum region. The fit to experimental data from the ALICE and ATLAS collaborations has, however, been limited to $p_{\perp} < 4 \text{ GeV}$, since at larger transverse momentum a perturbative QCD description is expected to account for the produced charged-hadron distribution from the non-equilibrium statistical approach used in this work. We have enhanced the relativistic drift-diffusion model of Ref. [2] using a rapidity-dependent diffusion, which produces a better description of the longitudinal spectra in the mid-rapidity region. The total reduced χ^2 indicates significantly improved model results at both $\sqrt{s_{NN}} = 2.76$ and 5.02 TeV . Extrapolating the model parameters to $\sqrt{s_{NN}} = 5.36 \text{ TeV}$, we have

also predicted the charged-hadron spectra for Run 3 at the LHC in the longitudinal and transverse directions.

Future developments of the model should include a microscopic derivation of the rapidity dependence of the diffusion coefficient, and possibly consider a transverse dependence as well. Including off-diagonal components in the diffusion matrix could also provide a better physical representation of charged-hadron production, but is certainly challenging to implement in the present solution scheme.

An extension to non-central collisions would require to consider the third spatial dimension, which would be problematic to tackle with spectral methods. The inclusion of the fragmentation sources is essential to describe baryon stopping, and could possibly be addressed in the spectral solution scheme by employing a different representation of the Fokker-Planck operator.

Acknowledgements We thank Johannes Hölck for discussions and remarks.

Declarations

- Availability of data and materials: The experimental data that are compared with our model calculations are available on <https://www.hepdata.net>. The model results shown in the figures are available from the authors upon reasonable request.
- Code availability: The Matlab-codes can be made available upon request.
- Authors' contributions: AR: Adapting the spectral eigenfunction method to the relativistic diffusion model, numerical solutions, plots; Writing - parts of the draft. GW: Concept, Methodology; Writing - parts of the draft; supervision, review and editing.

References

1. M. Arslanodk et al., *Hot QCD White Paper*, arXiv:2303.17254 (2023)
2. J. Hoelck, G. Wolschin, *Cylindrically symmetric diffusion model for relativistic heavy-ion collisions*, *Annalen Phys.* **236**, 2300307 (2024)
3. G. Wolschin, *Relativistic diffusion model*, *Eur. Phys. J. A* **5**, 85–90 (1999)
4. M. Biyajima, M. Ide, T. Mizoguchi, N. Suzuki, *Scaling behavior of $(N_{ch})^{-1} dN_{ch}/d\eta$ at $\sqrt{s_{NN}} = 130 \text{ GeV}$ by the PHOBOS collaboration and its implication: A possible explanation employing the Ornstein–Uhlenbeck process*, *Prog. Theor. Phys.* **108**, 559–569 (2002)
5. G. Wolschin, *Beyond the thermal model in relativistic heavy-ion collisions*, *Phys. Rev. C* **94**, 024911 (2016)
6. E. Fermi, *High energy nuclear events*, *Prog. Theor. Phys.* **5**, 570–583 (1950)
7. R. Hagedorn, *Hadronic matter near the boiling point*, *Nuovo Cim. A* **56**, 1027–1057 (1968)

8. F. Gelis, E. Iancu, J. Jalilian-Marian, R. Venugopalan, *The color glass condensate*, Annu. Rev. Nucl. Part. Sci. **60**, 463–489 (2010)
9. T. Koide, G.S. Denicol, P. Mota, T. Kodama, *Relativistic dissipative hydrodynamics: A minimal causal theory*, Phys. Rev. C **75**, 034909 (2007)
10. M. Luzum, P. Romatschke, *Conformal relativistic viscous hydrodynamics: Applications to RHIC results at $\sqrt{s_{NN}} = 200$ GeV*, Phys. Rev. C **78**, 034915 (2008)
11. B.H. Alver, C. Gombeaud, M. Luzum, J.Y. Ollitrault, *Triangular flow in hydrodynamics and transport theory*, Phys. Rev. C **82**, 034913 (2010)
12. U. Heinz, R. Snellings, *Collective flow and viscosity in relativistic heavy-ion collisions*, Annu. Rev. Nucl. Part. Sci. **63**, 123–151 (2013)
13. J.E. Bernhard, J.S. Moreland, S.A. Bass, *Bayesian estimation of the specific shear and bulk viscosity of quark-gluon plasma*, Nature Physics **15**, 1113–1117 (2019)
14. G. Nijs, W. van der Schee, U. Gürsoy, R. Snellings, *Transverse momentum differential global analysis and heavy-ion collisions*, Phys. Rev. Lett. **126**, 202301 (2021)
15. S. Bass, M. Belkacem, M. Bleicher, M. Brandstetter, L. Bravina et al., *Microscopic models for ultrarelativistic heavy ion collisions*, Prog. Part. Nucl. Phys. **41**, 255–369 (1998)
16. G. Wolschin, *Ultraviolet energy dependence of particle production sources in relativistic heavy-ion collisions*, Phys. Rev. C **91**, 014905 (2015)
17. Y. Mehtar-Tani, G. Wolschin, *Baryon stopping as a new probe of geometric scaling*, Phys. Rev. Lett. **102**, 182301 (2009)
18. Y. Mehtar-Tani, G. Wolschin, *Baryon stopping and saturation physics in relativistic collisions*, Phys. Rev. C **80**, 054905 (2009)
19. J. Hoelck, G. Wolschin, *Baryon stopping as a relativistic Markov process in phase space*, Phys. Rev. Res. **2**, 033409 (2020)
20. E. Abbas et al. (ALICE Collaboration), *Centrality dependence of the pseudorapidity density distribution for charged particles in Pb–Pb collisions at $\sqrt{s_{NN}} = 2.76$ TeV*, Phys. Lett. B **726**, 610–622 (2013)
21. J. Adam et al. (ALICE Collaboration), *Centrality dependence of the pseudorapidity density distribution for charged particles in Pb–Pb collisions at $\sqrt{s_{NN}} = 5.02$ TeV*, Phys. Lett. B **772**, 567–577 (2017)
22. S. Acharya et al. (ALICE Collaboration), *Transverse momentum spectra and nuclear modification factors of charged particles in pp, p–Pb and Pb–Pb collisions at the LHC*, J. High Energ. Phys. **2018**, 1–33 (2018)
23. G. Aad et al. (ATLAS Collaboration), *Measurement of charged-particle spectra in Pb+Pb collisions at $\sqrt{s_{NN}} = 2.76$ TeV with the ATLAS detector at the LHC*, J. High Energ. Phys. **2015**, 50 (2015)
24. F. Debbasch, K. Mallick, J.P. Rivet, *Relativistic Ornstein–Uhlenbeck process*, J. Statist. Phys. **88**, 945–966 (1997)
25. J. Dunkel, P. Hänggi, *Theory of relativistic Brownian motion: The (1+1)-dimensional case*, Phys. Rev. E **71**, 016124 (2005)
26. J. Dunkel, P. Hänggi, *Theory of relativistic Brownian motion: The (1+3)-dimensional case*, Phys. Rev. E **72**, 036106 (2005)
27. J. Łopuszański, *Relativisierung der Theorie der stochastischen Prozesse*, Acta Phys. Polon. **12**, 87–99 (1953)
28. R.M. Dudley, *Lorentz-invariant Markov processes in relativistic phase space*, Ark. Mat. **6**, 241–268 (1966)
29. R. Hakim, *Relativistic stochastic processes*, J. Math. Phys. **9**, 1805–1818 (1968)
30. G. Wolschin, M. Biyajima, T. Mizoguchi, N. Suzuki, *Time evolution of relativistic d + Au and Au + Au collisions*, Annalen Phys. **518**, 369–378 (2006)
31. G. Wolschin, *Particle production sources at LHC energies*, J. Phys. G **40**, 045104 (2013)
32. L. Gribov, E. Levin, M. Ryskin, *Semihard processes in QCD*, Phys. Rep. **100**, 1–150 (1983)
33. A. Mueller, J. Qiu, *Gluon recombination and shadowing at small values of x*, Nucl. Phys. B **268**, 427–452 (1986)
34. J. Blaizot, A. Mueller, *The early stage of ultra-relativistic heavy ion collisions*, Nucl. Phys. B **289**, 847–860 (1987)
35. L. McLerran, R. Venugopalan, *Computing quark and gluon distribution functions for very large nuclei*, Phys. Rev. D **49**, 2233–2241 (1994)
36. S. Acharya et al. (ALICE Collaboration), *Characterizing the initial conditions of heavy-ion collisions at the LHC with mean transverse momentum and anisotropic flow correlations*, Phys. Lett. B **834**, 137393 (2022)
37. K. Golec-Biernat, M. Wüsthoff, *Saturation effects in deep inelastic scattering at low Q^2 and its implications on diffraction*, Phys. Rev. D **59**, 014017 (1998)
38. D. Kharzeev, E. Levin, M. Nardi, *Color glass condensate at the LHC: hadron multiplicities in pp, pA and AA collisions*, Nucl. Phys. A **747**, 609–629 (2005)
39. D. Cubero, J. Casado-Pascual, J. and Dunkel, P. Talkner, P. Hänggi, *Thermal equilibrium and statistical thermometers in special relativity*, Phys. Rev. Lett. **99**, 170601 (2007)
40. F. Jüttner, *Das Maxwellsche Gesetz der Geschwindigkeitsverteilung in der Relativtheorie*, Annalen Phys. **339**, 856–882 (1911)
41. J.D. Bjorken, *Highly relativistic nucleus-nucleus collisions: The central rapidity region*, Phys. Rev. D **27**, 140–151 (1983)
42. E. Schnedermann, J. Sollfrank, U. Heinz, *Thermal phenomenology of hadrons from 200A GeV S+S collisions*, Phys. Rev. C **48**, 2462–2475 (1993)
43. C. Michael, L. Vanryckeghem, *Consequences of momentum conservation for particle production at large transverse momentum*, J. Phys. G: Nucl. Phys. **3**, L151 (1977)
44. R. Hagedorn, *Multiplicities, p_T Distributions and the Expected Hadron \rightarrow Quark - Gluon Phase Transition*, Riv. Nuovo Cim. **6N10**, 1–50 (1983)
45. K. Aamodt, et al. (ALICE Collaboration), *Production of pions, kaons and protons in pp collisions at $\sqrt{s} = 900$ GeV with ALICE at the LHC*, Eur. Phys. J. C **71**, 1655 (2011)
46. H. Zheng, X. Zhu, L. Zhu, A. Bonasera, *Systematic investigation of the particle spectra in heavy-ion collisions at the Large Hadron Collider*, Mod. Phys. Lett. A **35**, 2050177 (2020)
47. B.D. Shizgal, *Spectral Methods in Chemistry and Physics: Spectral and Pseudospectral Methods of Solution of the Fokker-Planck and Schrödinger Equations* (Springer, Dordrecht, 2015)
48. L.N. Trefethen, *Spectral Methods in MATLAB*, Software, Environments, and Tools (Society for Industrial and Applied Mathematics, 2000)
49. P.J. Davis, P. Rabinowitz, *Methods of Numerical Integration* (Academic Press, 2014)
50. W. Gautschi, *Orthogonal polynomials: Constructive theory and applications*, J. Comp. Appl. Math. **12–13**, 61–76 (1985)
51. R. Blackmore, B. Shizgal, *Discrete-ordinate method of solution of Fokker-Planck equations with nonlinear coefficients*, Phys. Rev. A **31**, 1855–1868 (1985)
52. B.D. Shizgal, H. Chen, *The quadrature discretization method (QDM) in the solution of the Schrödinger equation with non-classical basis functions*, J. Chem. Phys. **104**, 4137–4150 (1996)

-
53. K. Leung, B.D. Shizgal, H. Chen, *The quadrature discretization method (QDM) in comparison with other numerical methods of solution of the Fokker–Planck equation for electron thermalization*, J. Math. Chem. **24**, 291–319 (1998)
 54. H. Risken, *The Fokker–Planck Equation: Methods of Solution and Applications*, Vol. 18 of *Springer Series in Synergetics* (Springer Berlin, Heidelberg, 1996)
 55. B.D. Shizgal, *Pseudospectral solution of the Fokker–Planck equation with equilibrium bistable states: the eigenvalue spectrum and the approach to equilibrium*, J. Stat. Phys. **164**, 1379–1393 (2016)
 56. A. Schulze-Halberg, *Darboux transformations for (1+2)-dimensional Fokker–Planck equations with constant diffusion matrix*, J. Math. Phys. **53**, 103519 (2012)
 57. B. Abelev et al. (ALICE Collaboration), *Centrality dependence of π , K, and p production in Pb–Pb collisions at $\sqrt{s_{NN}} = 2.76$ TeV*, Phys. Rev. C **88**, 044910 (2013)
 58. S. Acharya et al. (ALICE Collaboration), *Production of charged pions, kaons, and (anti-)protons in Pb–Pb and inelastic pp collisions at $\sqrt{s_{NN}} = 5.02$ TeV*, Phys. Rev. C **101**, 044907 (2020)
 59. R. Baier, Y. Dokshitzer, A. Mueller, S. Peigné, D. Schiff, *Radiative energy loss and p_{\perp} -broadening of high energy partons in nuclei*, Nucl. Phys. B **484**, 265–282 (1997)
 60. X. Guo, X.N. Wang, *Multiple scattering, parton energy loss, and modified fragmentation functions in deeply inelastic eA scattering*, Phys. Rev. Lett. **85**, 3591–3594 (2000)
 61. K.M. Burke et al. (JET Collaboration), *Extracting the jet transport coefficient from jet quenching in high-energy heavy-ion collisions*, Phys. Rev. C **90**, 014909 (2014)
 62. J.C. Lagarias, J.A. Reeds, M.H. Wright, P.E. Wright, *Convergence properties of the Nelder–Mead simplex method in low dimensions*, SIAM J. Opt. **9**, 112–147 (1998)
 63. J. D’Errico, *Adaptive robust numerical differentiation*, MATLAB Central File Exchange (2023)
 64. D.M. Röhrscheid, G. Wolschin, *Centrality dependence of charged-hadron pseudorapidity distributions in PbPb collisions at energies available at the CERN Large Hadron Collider in the relativistic diffusion model*, Phys. Rev. C **86**, 024902 (2012)